



Percolation and conductivity development of the rod networks within randomly packed porous media

Mingzhi Wang^{a,b,c,e,*}, Yushi Liu^{a,b,c}, Beimeng Qi^{d,**}, Abir Al-Tabbaa^e, Wei Wang^{a,b,c}

^a School of Civil Engineering, Harbin Institute of Technology, Harbin, 150090, China

^b Key Lab of Structures Dynamic Behavior and Control of the Ministry of Education, Harbin Institute of Technology, Harbin, 150090, China

^c Key Lab of Smart Prevention and Mitigation of Civil Engineering Disasters of the Ministry of Industry and Information Technology, Harbin Institute of Technology, Harbin, 150090, China

^d College of Quality & Safety Engineering, China Jiliang University, Hangzhou, 310018, China

^e Department of Engineering, University of Cambridge, Cambridge, CB2 1PZ, UK

ABSTRACT

A percolation-permeation-diffusion simulation and analysis scheme was proposed with Cellular Automata (CA) and Lattice Boltzmann method (LBM). The interconnection and transport properties of the carbon nanotube (CNT) network in the porous composite were investigated with the proposed scheme. The physical system was modelled as the rod-particle composite with an adjustable packing density of the porous medium, and experiment on the electrical resistivity development was conducted on the CNT-cement composite. A general trend that increased network content increased the electrical conductivity was observed both numerically and experimentally. The simulation-based study demonstrates that the densely packed porous medium can further enhance the connectivity and conductivity of the network within, especially with the shortened rod length. Representative elementary volume analysis was performed to determine the suitable size of the digital sample. It was found that heterogeneity caused locally enhanced transportability. The hydration product covering the CNT surface can introduce surface resistance to increase the elementary resistivity of the network to a magnification of tens times. The proposed simulation-analysis scheme is a generic method to evaluate the conductive network formed in porous media.

1. Introduction

Attention attracted in 1992 [1], carbon nanotube (CNT) has been adopted to produce multifunctional composite due to its outstanding features of high strength, large surface area and fine conductivity. Such implement includes but not limited to CNT-grown bone [2], CNT-based gas sensors [3] and damage sensors [4], CNT-based anti-freezing treatment [5], CNT-based catalysts [6] and CNT-enhanced cement and ceramic [7,8]. More recently, CNT-cement composite was used as a medium for the electrical curing method proposed to solve the problem of construction under sub-zero temperature [9]. The previous study demonstrated that the conductive properties of the CNT network in a composite were majorly influenced by the dimension, shape, agglomeration, homogeneity and spatial density of the CNTs. Increased CNT content in a composite caused enhanced electrical conductivity, and the electrical conductivity development followed a percolation scaling law in terms of the CNT content [10]. More homogeneous CNT dispersion reduced the electrical percolation threshold [11]. The CNT conglomeration increased electrical resistivity [12]. CNT network simulated with a

morphology of tumble-weed presented a similar CNT content required to achieve the peak conductivity as the rod network model [13]. The CNT percolation threshold increased with the decreasing aspect ratio, which as well significantly influence the disentanglement and the homogeneity [14]. A net reduction in the simulated water permeability variance was observed with the increased CNT length [15], indicating that extended rod length is in favour of the conductivity development. The above pioneering work revealed the morphological dependence of the CNT on the conductivity development of the CNT network to a large extent. However, the CNT network in most of the application exists in the form of composite. The influence of the surrounding porous medium on the CNT network formed within can still be further explored. In this paper, we demonstrate a simulation-based study to investigate the percolation behaviour and the conductivity development of the CNT-particle composite. The composite system was modelled as the rod-like network in a random porous medium with varying packing density. Cellular Automata (CA) [16] and Lattice Boltzmann method (LBM) [17] were adopted as the basic algorithms to conduct the percolation analysis, permeation simulation and diffusion simulation

* Corresponding author. School of Civil Engineering, Harbin Institute of Technology, Harbin, 150090, China.

** Corresponding author.

E-mail addresses: mwang@hit.edu.cn (M. Wang), qbm@cjl.u.edu.cn (B. Qi).

with the same model. The 3D compatible CA-LBM simulation scheme was originally proposed as a generic tool to conduct transport analysis on the 3D composite with adjustable porous medium. The aim of this study is to numerically observe the conductivity and connectivity development before and after the percolation threshold of the rod network in differently packed pore structures.

The insulator-to-conductor transition, which is a result of the electrical percolation, through the increment of the conductive content in a composite was majorly referenced as the mechanism of the electrical conductivity development [8,13,18,19]. In percolation theory [20], the percolation threshold (P_g) denotes the minimum volumetric fraction of particles to form a global connection in the whole volume, in which a path can be found to connect every individual particle. Additionally, there exist a volumetric fraction of the particles to form a single path connecting one end of the volume to the opposite end, namely the subcritical percolation threshold (P_s). A conductive network in a composite can be treated as an insulator when the conductive volume fraction is below P_s since there is no electron migration path connecting the two macroscopic ends. In a percolation analysis, a fraction of connection is defined as the ratio of the volume of the connected particles to the volume of all the particles [21]. The fraction of connection was used to describe the percolation development of a connected system. A connected fraction of 100% is maintained when the volume content is above the percolation threshold [22,23]. Due to the complexity of obtaining the analytical solution, the percolation problem was often solved with simulation-based approaches. The algorithms involved can be categorized into discrete methods [24,25] and continuous methods [26,27]. Among the discrete methods, by John von Neumann [28] proposed CA as a class of algorithms, which was used for the percolation analysis in 2D discrete systems [29,30]. Percolation behaviour can explain the conductivity development of a network to some extent. However, it is open to question that the content range up to the percolation threshold [31] is sufficient to cover the entire content range of the mass/electron transport. Physically, a sudden increment of the permeability of the connected pores can be observed when the percolation threshold is exceeded, and the permeability will continuously rise with the increment of the conductive content [21]. In this sense, computational fluid dynamics (CFD) can further describe the transportability above the percolation threshold.

The CFD-based simulations include three well-established methods, namely the Navier-Stokes solver [32,33], the discrete element method [34,35] and LBM [17,36]. Mechanical models on the contact behaviour of the nano-composite are facing a major challenge. The current bottleneck is the analytical description of the movement of deformable objects with irregular shape [37]. In this study, the 3D conductive phase in the random porous medium can hardly, if not impossible, be described with analytic geometry. Therefore, the lattice-based LBM is more suitable to realise the task than the Navier-Stokes solver and the discrete element method, which requires analytic boundary description. The discrete feature of LBM makes it in natural compatibility with 3D image-based model of composite material [38]. Comparing with models without 3D spatial consideration [39,40], mass migration simulated with LBM models can provide full-map velocity distribution through the volume of the composite [41]. In the previous study of LBM, permeative flow was realized with D2Q9 model [42,43], D3Q7 model [44] and D3Q19 model [45]. The DxQy denotes that the lattice system was described with x dimensions and y directions of velocities [17]. It was assumed by the above models that the permeation was conducted with a single fluid phase, therefore the multi-phase modelling was rarely addressed. On the other hand, the practical fluid in diffusion phenomenon often exists in the form of solution. Therefore, the simulation of diffusive fluid inevitably requires the mathematical description of the multi-phase fluid. By assuming that the concentration of the solute is too small to influence the velocity development of the solvent, Kang [46,47] realized a multi-phase D2Q9 model to simulate the diffusive fluid driven by the concentration difference.

Experimentally, the diffusion was also intensively studied for the electrical conductivity development with formation factor analysis [48–50]. The electrical formation factor was defined as the ratio of the conductivity of the network to the conductivity of the elementary phase of the network. The diffusive formation factor was defined as the ratio of the diffusion coefficient of the network to the diffusion coefficient of the bulk phase of the network. The electrical conduction can be treated as the result of the diffusive migration of the electrons. As a result, the electrical formation factor is identical to the electrical formation factor [50,51]. The formation factor development of porous media was both experimentally and analytically proved to follow Archie's law [49,52]. In this study, the phase of interest is the rod network within the random porous medium. Since both the pores and the rod network can contribute to the electron transport, the experimental study of the system with current permeation and diffusion techniques can hardly meet the requirement of control variates. Meanwhile, a simulation-based study can straightforwardly perform the permeation and diffusion on a specific network in the composite. Therefore, the above-mentioned philosophy on the conductivity of porous media can be inherited to the simulated rod network within the pore structure. The D3Q19 multi-phase LBM model in this study was proposed based on the previous study [45,47] to independently conduct the permeation and diffusion simulation in one system.

A more generally confronted problem of the numerical study is the statistic flocculation introduced by the heterogeneity, when the digital sample size is not large enough. A representative elementary volume (REV) [53] analysis can aid to determine the size of the digital samples so that a certain macroscopic property of the heterogeneous sample can result in relatively stable value. A common method to determine the REV size is through tuning the sample size until a Chi-square criterion is fulfilled with the property of interest [54,55] such as volumetric content. The previous study on the 3D modelling of the composite may not address the issue of representativity [56,57], but the importance of the REV analysis is increasingly emphasized in more recent numerical study [58,59] and image-based study [60,61]. In this work, the REV analysis was first of all performed with algorithm-generated composite with Wang's model [62]. The pore structure was tuned with different packing status, which was random close packing (RCP), random loose packing (RLP) and random sequential addition (RSA). RCP was defined as the random packing status with the highest packing density [63]. RLP was defined as the stable random packing status with the packing density lower than the RCP [64]. RSA was defined as the non-packing status of the particles simulated with the random placement method [65,66].

2. Methodology

2.1. Overview

Fig. 1 demonstrates the flow chart the numerical simulation and analysis. Particle packing simulation [67] was initially conducted to generate the initial pore structure formed by particles. Rod network was then randomly placed in the porous medium and further extracted from the composite. REV analysis was conducted on the rod network to determine the digitized sample size. The percolation analysis was performed to identify the percolation threshold (P_g) and the subcritical percolation threshold (P_s) of the extracted rod network. Permeation and diffusion simulation were conducted through the rod network between the volumetric fraction range of (P_s , 100%). Details regarding each step are presented in the following sections.

2.2. Pore structure reconstruction

Particle packing simulation was conducted with Wang's model [62] as illustrated by Fig. 2. A mono-size distribution was assigned to the particles with an average radius of 8 lattice unit length (lu) so that the influence of particle size distribution is fixed. The length mapping was 1

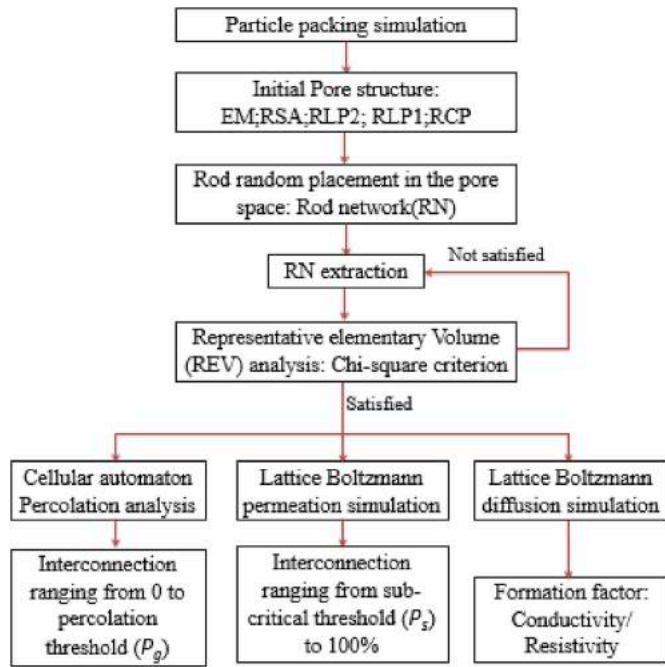


Fig. 1. Simulation and analysis flowchart of this study.

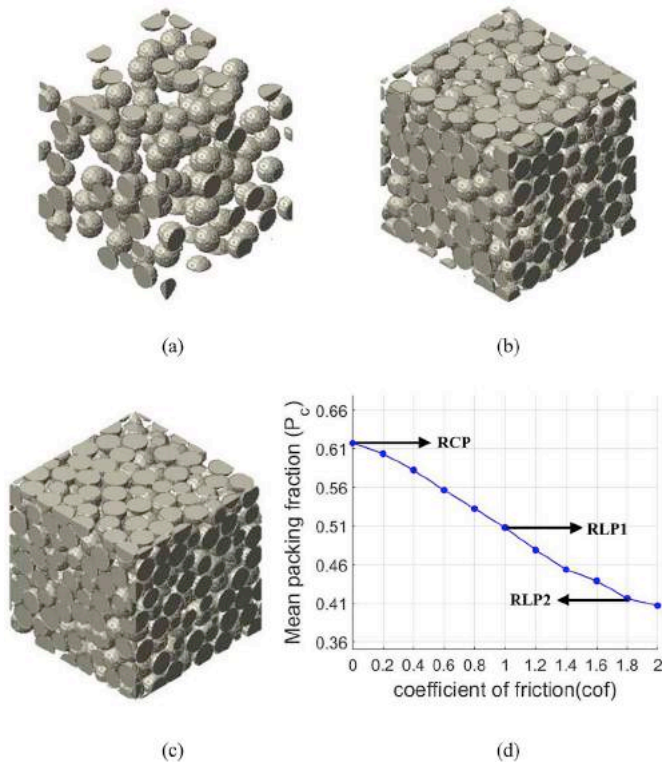


Fig. 2. (a) RSA pore structure. (b) RLP1 pore structure. (c) RCP pore structure. (d) User-specified packing density through the tuning of the friction coefficient.

$\mu\text{m}/\text{lu}$. The coefficient of friction was used as the tuning parameter to obtained pore structures with user-specified porosity as presented in Fig. 2 (d). In this study, digital samples were generated with labels of RCP, RLP1, RLP2 and RSA. The rod network placed in a completely empty 3D domain, labelled as EM, was also conducted for comparison. The generated packed structures were voxelized for the following LBM simulation with cubic lattice. Void ratio and packing fraction were

calculated by Eqs. (1) and (2), respectively.

$$P_v = \frac{N_{EV}}{N_v} \quad (1)$$

$$P_c = \frac{N_{CV}}{N_v} = 1 - P_v \quad (2)$$

Where P_v is the void ratio, P_c is the packing fraction, N_{EV} is the pore volume, N_{CV} is the particles volume and N_v is the sample volume. The particle packing simulation was conducted with 15,000 particles in a $320 \times 320 \times 2300$ domain. In this study, the RLP1 structure was generated following the commonly recognized definition of the random loose packing, which is the stable packed status with the minimum packing fraction and a coordination number of 4. The RLP2 porous medium is a mechanically unstable structure with a packing fraction lower than the RLP1.

2.3. 3D spatial distribution of the network

The random porous medium with different packing density was adopted as the initial boundary for the placement of the rod network as presented in Fig. 3(a). Random sequential addition was applied to each individual rod, in which random centroid coordinates and rotational degrees were randomly assigned following a uniform distribution. Rod-rod and rod-particle overlapping were prohibited through the re-assignment of the coordinates and rotational degrees when overlapping was detected. The volumetric fraction of the rod network was calculated with Eq. (3).

$$v_t = \frac{\sum_{i=1}^n v_i}{N_v} \quad (3)$$

Where v_t is the volumetric fraction of the rods, v_i is the individual volume of the i th rod and n is the total number of the added rods. 3D samples only containing the rod network were then extracted and stored for the CFD simulation/analysis as presented in Fig. 3(b). REV analysis was conducted on the extracted rod network with the chi-square criterion [54,55], of which the property of interest is the volumetric content.

2.4. Percolation analysis

The percolation analysis in this study applied a 3D CA ‘burning’ algorithm. During the initialization step of the analysis, ‘fire’ voxels were assigned in one end of the extracted rod network as presented in Fig. 4 (a). The solid phase of the rod network in the original sample was defined as ‘combustible’ voxels. The ‘combustible’ voxels in the 3D Moore neighbours [16] of the ‘fire’ voxels were set ‘on fire’ in each iteration as presented in Fig. 4(b). The above neighbour-checking and

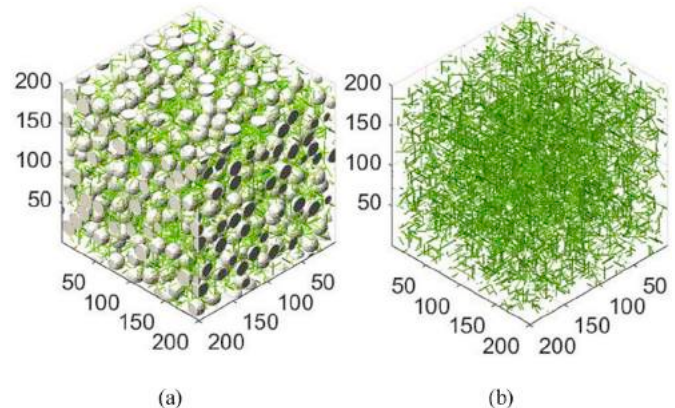


Fig. 3. (a) A rod network placed in the RSA pore structure (b) A extracted rod network after the placement.

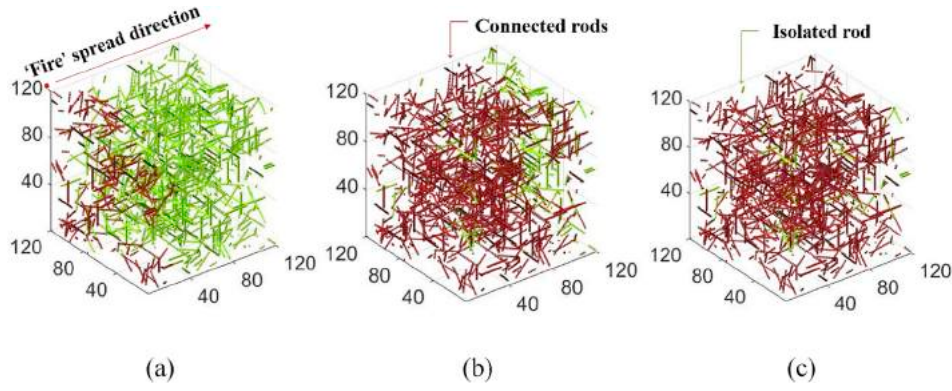


Fig. 4. (a) Initialization step. (b) 'Fire' progression. (c) Isolation and connection.

burning process were repeated until the amount of 'fire' voxels was stable between two iterations as illustrated in Fig. 4(c). The fraction of connected was then calculated with Eq. (4).

$$F_c = \frac{V_c}{\sum_{i=1}^n V_i} = 1 - \frac{\sum_{i=1}^n V_{iso}}{\sum_{i=1}^n V_i} \quad (4)$$

Where F_c is the volumetric fraction of connected rods, V_c is the volume of the connected rods and V_{iso} is the individual volume of an isolated-rod. The percolation threshold P_g was defined as the vt_i with which F_c reaches 100% for the first time. At the percolation threshold, at global rod network was formed within the volume and there always was a connected path between two arbitrary rods. The subcritical threshold P_s was defined as the vt_i with which a single connected passage was formed between the two opposite ends of the volume for the first time. As a discrete method, the computation demand majorly depends on the volume size and resolution. This method is viable for the experimentally obtained images including 2D backscattered electron and 3D computed tomography images due to its voxel-based nature.

2.5. Permeation simulation

The permeation simulation was conducted on the REV of the pore structures and rod network with LBM fluid as illustrated in Fig. 5. The REV was expanded in the two ends of the X-axis and periodic boundary condition was applied to the rest four ends. The conductive volume in the REV was initially filled with uniformly distributed solvent phase. A high solvent density was maintained in one expanded volume as fluid

inlet volume, and a low solvent density was maintained in the outlet volume. The rod network as illustrated by Fig. 3(b) was defined as the only permeable phase for the D3Q19 LBM simulation. The density difference was calculated with Eq. (5) with the Murnaghan model [68].

$$P = \frac{K_0}{n} \left[\left(\frac{\rho}{\rho_0} \right)^n - 1 \right] + p_0 \quad (5)$$

Where P is the pressure within the given volume, p_0 is the reference pressure, ρ_0 is the reference density, n is a parameter related to the material and K_0 is the bulk modulus. By applying Eq. (5) on the inlet and outlet volume of the digital sample, the pressure difference can then be calculated with Eq. (6).

$$\Delta p_z = p_{inlet} - p_{outlet} = \frac{K_0}{n} \left[\left(\frac{\rho_{inlet}}{\rho_0} \right)^n - \left(\frac{\rho_{outlet}}{\rho_0} \right)^n \right] \quad (6)$$

Where Δp_z is the pressure difference, p_{inlet} is the pressure in the inlet volume, p_{outlet} is the pressure in the outlet volume, ρ_{inlet} is the density in the inlet volume and ρ_{outlet} is the density in the outlet volume. Pure water was set as the solvent phase with $K_0 = 2.15$ GPa and $n = 7.15$ [68]. The initial density of the solvent was calculated as the reciprocal of the molar volume of water as $\rho_0 = 5.56e - 14$ mol/ μm^3 . Constant densities were applied to the expanded volumes with $\rho_{inlet} = 2\rho_0$ and $\rho_{outlet} = 0.5\rho_0$. The resulted pressure difference calculated with Eq. (6) was 5.4578Gpa. In the LBM simulation, the 3D density distribution of the solvent phase was described with Eqs. (7) and (8), [17].

$$f_i(\mathbf{x} + \mathbf{e}_i \delta t, t + \delta t) - f_i(\mathbf{x}, t) = - \frac{f_i(\mathbf{x}, t) - f_i^{eq}(\mathbf{x}, t)}{\tau} \quad (7)$$

$$f_i^{eq}(\mathbf{x}, t) = w_i \rho \left[1 + \frac{\mathbf{e}_i \cdot \mathbf{u}}{c_s^2} + \frac{(\mathbf{e}_i \cdot \mathbf{u})^2}{2c_s^4} - \frac{\mathbf{e}_i \cdot \mathbf{u}}{2c_s^2} \right] \quad (8)$$

Where i is the direction of the discrete velocity, \mathbf{x} is the position of the lattice, t is the time of the fluid evolution, $f_i(\mathbf{x}, t)$ is the current density distribution of the fluid, $f_i^{eq}(\mathbf{x}, t)$ is the equilibrium density distribution resulted from $f_i(\mathbf{x}, t)$, w_i is the weight factor, ρ is the macroscopic density; \mathbf{u} is the macroscopic velocity; c_s^2 is the lattice sound speed and τ is the relaxation time. In the D3Q19 single relaxation time simulation, c_s^2 was set to be $c_s^2 = \frac{8x}{3\delta t} = \frac{1}{3}$, τ was the set to be $\tau = 1$ and i was an integer between 0 and 18 [69,70]. The simulation was conducted until a steady-state flow was formed when the difference of the average velocity of the whole network between two iterations is less than 0.2% of the current average velocity. The intrinsic permeability was calculated with Eq. (9) as Darcy's law [71] in LBM system [17].

$$K = \frac{v_{Qz} L_z}{A_{x-y} \Delta p_z} = \frac{v}{\Delta p_z} \cdot L_z \bar{u}_z = \frac{v}{\Delta p_z} \cdot N_z \frac{\sum_{i=1}^{N_x} \sum_{j=1}^{N_y} \sum_{k=1}^{N_z} u_z(i, j, k)}{N_x \cdot N_y \cdot N_z} \quad (9)$$

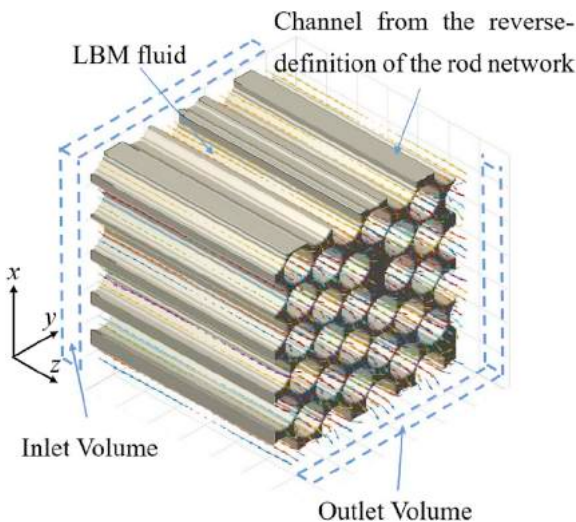


Fig. 5. Solid-phase boundaries from the reverse definition of TN.

Where $K(m^2)$ is the intrinsic permeability or water permeability, ν is 1.002×10^{-3} Pa·s as the dynamic viscosity of water at 20 °C, $Q_z(m^3/s)$ denotes the flowrate in the z-direction, $A_{x-y}(m^2)$ denotes the cross-sectional area in the xy-plane, $\bar{u}_z(m/s)$ is the mean velocity in the z-direction, $L_z(m)$ is the length of the sample in the z-direction, $u_z(i, j, k)$ LBM velocity distribution, N_x, N_y and N_z are the number of lattices in x, y and z-direction, respectively [45]. provided a time mapping of $T_0 = 4.15 \times 10^{-8}$ s/lt when the length mapping was $L_0 = 1 \mu m/lu$ for water permeation simulation. In LBM system, lu is the LB unit length and lt is the LB unit time.

2.6. Diffusion simulation

The solute part of the multi-component LBM was defined to simulate the diffusive flow independently from the permeation simulation. The density of the solute phase was set to be a uniformly distributed value of 3.30×10^{-17} mol/ μm^3 over the network with the molar volume of dissolved CO_2 . 105% density was maintained in the inlet volume and 95% density was maintained in the outlet volume. The above setting resulted in a 10% density/concentration difference between the two expanded volumes, which derived the diffusive migration of the solute in the LBM system. In addition to Eqs. (7) and (8), the 3D density distribution of the solute phase was given by Eq. (10)–(11) [72].

$$g_i^s(\mathbf{x} + \mathbf{e}_i \delta t, t + \delta t) - g_i^s(\mathbf{x}, t) = -\frac{g_i^s(\mathbf{x}, t) - g_i^{s, eq}(\mathbf{x}, t)}{\tau_s} \quad (10)$$

$$g_i^{s, eq}(\mathbf{x}, t) = w_i C^s \left[1 + \frac{\mathbf{e}_i \cdot \mathbf{u}}{c_s^2} + \frac{(\mathbf{e}_i \cdot \mathbf{u})^2}{2c_s^4} - \frac{\mathbf{e}_i \cdot \mathbf{u}}{2c_s^2} \right] \quad (11)$$

Where g_i^s is the density distribution of sth solute; $\tau_s = 1$ is the relaxation time for the calculation of the sth solute and C^s is the concentration of the sth solute defined by Eq. (12), [72].

$$C^s = \frac{\sum_{i=1}^{19} g_i^s}{\sum_{i=1}^{19} f_i} \quad (12)$$

The flux through a cross-section area in the y-z plane is given by Eq. (13) according to Fick's first law [73],

$$J_{y-z} = -D_x \frac{\delta \phi}{\phi x} = -D_x \frac{\Delta C^s}{L_x} \quad (13)$$

Where $\frac{\delta \phi}{\phi x}$ is the concentration gradient in the x-direction, D_x is the coefficient of diffusion, J_{y-z} is the flux through the area of measurement in the y-z plane, ΔC^s is the concentration difference and L_x is the length between the concentration difference. The area of measurement was set to be the middle cross-section of the REV at $x = \frac{x_{REV}}{2}$, where x_{REV} is the sample size in the x-direction. The formation factor [48,51] was calculated with the measured flux in the LBM system as given by Eq. (14). The condition of applying Eq. (14) is that the ΔC^s and L is the same in D_0 and D_e , which can be directly defined in a simulation.

$$F(vt) = \frac{D_0}{D_e} = \frac{J_0 \frac{L_x}{\Delta C^s}}{J_e(vt) \frac{L_x}{\Delta C^s}} = \frac{J_0}{J_e(vt)} = \frac{\sum_{i=1}^{N_y} \sum_{j=1}^{N_z} u_{g,x,0}(i, j, k = \frac{N_{REV}}{2})}{\sum_{i=1}^{N_y} \sum_{j=1}^{N_z} u_{g,x,e}(i, j, k = \frac{N_{REV}}{2})} \quad (14)$$

Where J_0 is the base flux through the bulk(EM), $J_e(vt)$ is the flux through RN a volumetric fraction of vt , $u_{g,x,0}$ is the velocity distribution in the bulk(EM) and $u_{g,x,e}$ is the velocity distribution through the rod network. The steady-state of the measurement in the formation factor analysis was defined as the state when the concentration difference between the iteration was within $1.2 \times 10^{-3}\%$.

The above simulation scheme is a generic simulation routine developed to study the conductive network in a composite. The same routine can be applied to different morphology-based inclusion such as

graphene nanoplatelets and carbon particles. The initial LBM parameters can be maintained to establish a cross-material comparison. The engine were independently programmed with MATLAB^(R) [74].

2.7. Example experiments

An experiment was conducted as an example of the electrical conductivity development of a CNT network in the composite. The CNT added to the ordinary Portland cement mortar has recorded length, diameter and electrical resistivity of 20 μm , 100 nm and 0.78 Ω cm, respectively. Fine silica sand with an average grain size of 1.18 mm and fineness modulus of 2.41 was adopted as the aggregate. The composite of the experiment is a multiscale system containing the mesoscale sand-pore and the microscale cement-pore-CNT, and the simulation focused on the later. In order to increase the homogeneity of the CNT dispersion, an initial dry mixing process was conducted on the CNT and sand in an agitator for 3min. Cement particles were then added to the mixture, followed by the addition of superplasticizer and water in the following 5min wet mixing process. Fig. 6 presents the electrical resistance measurement of the fresh sample. The mixture was moulded in 40 mm \times 40 mm \times 160 mm mortar. Two area electrodes with a size of 40 mm \times 60 mm were placed in the fresh mortar for the measurement of the electrical resistance. The electrical resistivity ρ was calculated with $\rho = RS/L$, where R is the measured electrical resistance, $L = 140$ mm and $S = 40 \times 40$ mm². The measurement was conducted with a Tonghui TH2811D Digital Multimeter (Changzhou Tonghui Electronic Co., Ltd.). An alternative measurement following a similar principle can be found in Ref. [75]. Scanning electron microscope (SEM) was conducted with merlin compact (Carl Zeiss AG). Table 1 presents the proportion of the composite.

3. Result and discussion

3.1. REV analysis

Fig. 7 presents the REV analysis with the volume fraction of the rod network as the property of interest. The result of the network placement in the empty volume (EM) is presented by Fig. 7(a). It can be noticed that the improvement of the representativity can be intuitively observed with an increasing volume size of the EM simulation. Fig. 7(b)–(e) and Table 2 presents a comparison of the network placed in the other porous media. The comparison indicates that the reduced porosity increased the REV size requirement of the digital sample. The chi-square values from the EM, RSA, RLP1 and RCP samples indicates that the representativity increased with the increment of the packing density. Increasing the individual rod length does not present a clear pattern of chi-square development. A much higher chi-square value from the RLP2 porous medium can be observed, indicating a more severe statistical flocculation and heterogeneous network distribution as reflected by Fig. 7(e). All the chi-square values drop below 10^{-4} when the domain size reaches 120 μm except for the RLP2 samples. As a result, a volume size of $120 \times 120 \times 120$ was adopted to represent the network in EM, RSA, RLP1 and RCP samples in the following study. The RLP2 groups adopted the same volume size to observe the data development in the non-representative

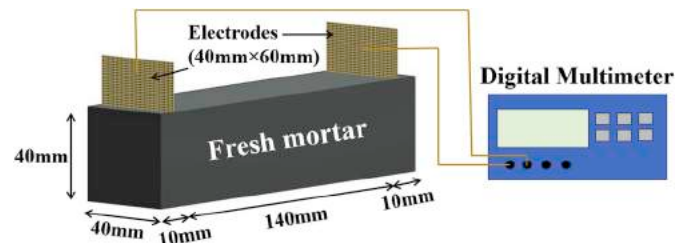


Fig. 6. The electrical resistance measurement conducted experimentally.

Table 1

Mixing proportions of cement/CNT composites in the experiment.

Water/Cement ratio	Cement/Sand (Mass ratio)	CNT concentration (CNF/Cement)
0.35	1:1	0
0.35	1:1	0.5 vol%
0.35	1:1	1.0 vol%
0.35	1:1	1.5 vol%
0.35	1:1	2.0 vol%
0.35	1:1	2.5 vol%

and heterogeneous samples. In comparison, the grey dot line in Fig. 7 presents the critical REV criteria ($L_{REV} = 4L$) from an image-based study of the carbon fibres [60,61]. The REV size determined with this work is higher since stricter criterion was applied. The incorporation of the porous medium can increase REV requirement as illustrated by RLP2 group.

3.2. Percolation analysis

Fig. 8(a) presents the percolation development with varying network volumetric fraction and rod length. It can be observed that the extended rod length enhances the rod interconnection, which is reflected by the decreasing percolation threshold. Fig. 8(b) presents the percolation development of the network in different porous media. The percolation threshold appears to be independent of the void ratio, but the process to form a global connection is influenced by the packing status. Before the formation of the global interconnection, the network in more densely packing porous medium demonstrates a more rapid development of the fraction of connection. Exceptionally, the RLP2 sample presents the highest fraction of connection in the pre-percolation stage.

The above results indicate that the densely packed porous medium is

in favour of the formation of the connected network within. The available volume for the rod placement in the RCP was the smallest, leading to an increased ratio of the network volume to the pore volume. Therefore, the local concentration of the network in RCP was the highest among all the simulations under the same network content, causing the improved interconnection of the network in limit pore space. Another influence reflected by the results was the spatial distribution of the pores. As discussed in the REV analysis, RLP2 had the most heterogeneous pore structure. The heterogeneous feature indicates that the pores in RLP2 sample were partially concentrated in certain areas rather than homogeneously distributed. Therefore, the rods in RLP2 porous medium must have increased possibility to be placed in these assembled pores, and the rod isolation in these areas was reduced. In this sense, the increased packing fraction and the heterogeneously distributed network are in favour of the fraction of connection development of the rod network.

Fig. 9 presents the percolation threshold development regarding the individual rod length. P_g denotes the percolation threshold of the network and P_s denotes subcritical threshold of the network. P_s is a value formed in the pre-percolation stage when the first conductive path

Table 2

Chi-square values calculated from the REV analysis.

RN structure	Sample sizes and corresponding chi-square value (10^{-4})					
	20 μm	40 μm	60 μm	80 μm	100 μm	120 μm
REV-EM-L22	127.5	5.7	3.3	2.6	1.2	0.3
REV-EM-L18	56.5	4.5	1.1	0.2	0.6	0.1
REV-EM-L14	126.6	17.2	6.2	4.3	1.7	0.8
REV-RCP-L18	227.2	20.1	2.8	2.8	2.5	0.8
REV-RSA-L18	88.9	13.9	3.0	1.4	1.1	0.5
REV-RLP1-L18	82.6	23.7	10.2	1.5	1.6	0.6
REV-RLP2-L18	386.5	290.1	107.4	42.6	13.3	3.6

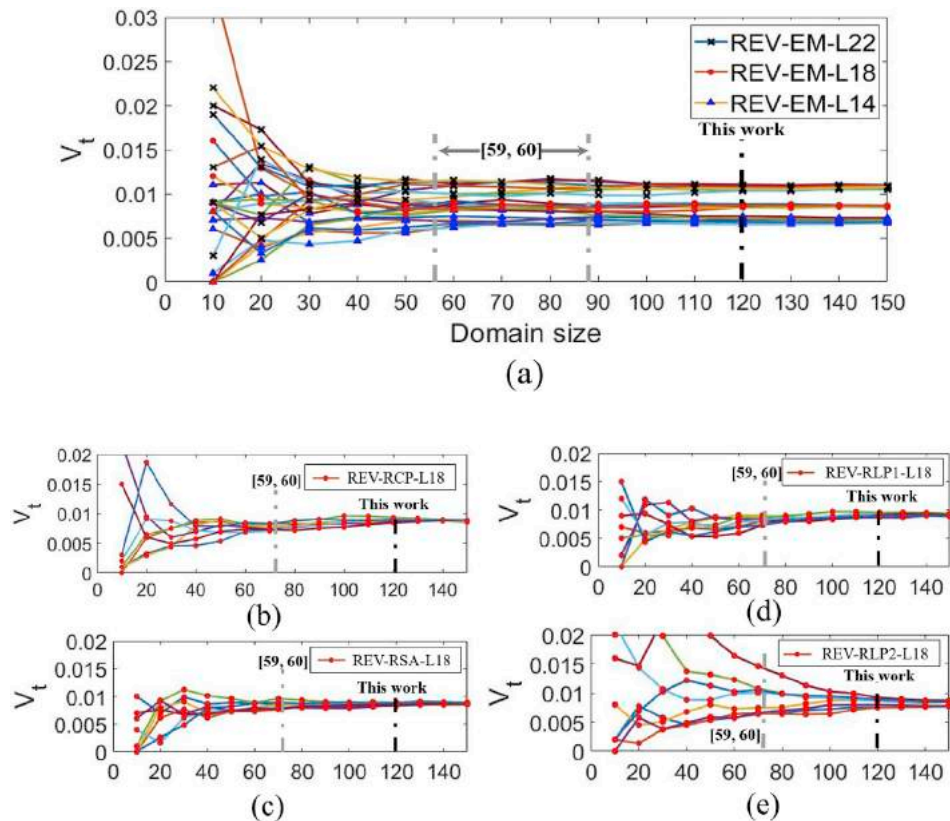


Fig. 7. REV analysis of the network in (a) the EM space, (b) the RCP pore structure, (c) the RSA pore structure, (d) the RLP1 pore structure and (e) the unstable RLP2 pore structure.

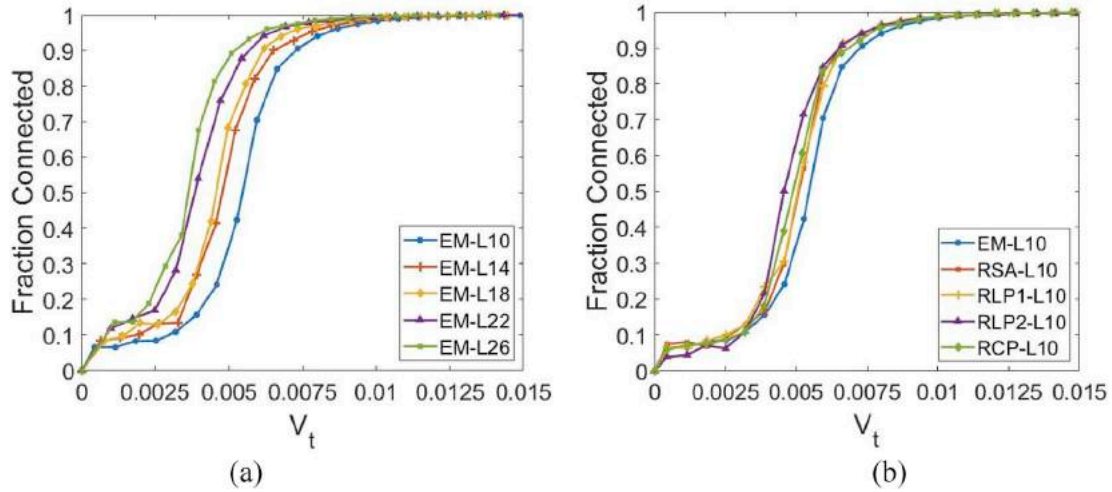


Fig. 8. Percolation analysis of (a) EM samples with different length and (b) L10 samples in different pore structures.

begins to be able to run through the REV. The percolation threshold was in negative correlation with the length of the individual rod. The subcritical value demonstrates a similar correlation with the rod length but the dependence of void ratio is more significant. A clear pattern can be found that the lower packing density resulted in higher P_s , indicating that the connection path through the sample was harder to form in a loosely packed porous medium. The EM- P_g function indicates that rod network processes a percolation threshold range of 0.0018–0.0201 (0.18–2.01 vol%) within the length range of 1–1000lu. In comparison, a percolation threshold range of 0.1–1.5 wt% was reported with various composites with CNT [76–79]. The density of the substance involved in the previous study was not exactly the same, but an estimated range of 0.2–3 vol% can be converted by assuming 1 vol% = 2 wt%. Beside the above experimental data, the analytical study [80] also demonstrated a CNT percolation threshold down to 0.2 vol% (2×10^{-3}). The proposed CA model was mathematically based on the fraction of connection development in the 3D matrix of a composite. Confirmative detection of the isolated phase was realized as presented in Fig. 4(c). The algorithm is as well suitable for the analysis with experimental obtained 3D structure such as Computed Tomography images. The image-based analysis can provide a direct measurement of the percolation status over the volume, comparing with the previous indirect measurement with mass weighting.

3.3. Permeation simulation

Fig. 10 (a) presents the permeation simulation results with an individual rod length of 20lu. The percolation threshold of the network was $P_g = 0.72\%vol$ from the EM- P_g function, and the subcritical threshold was $P_s = 0.50\%vol$ from the EM- P_s function. The permeation simulation result reflects a general trend that the permeability of the network increases with the increment of the content. A steep increment of the permeability can be noticed near the percolation threshold, and the subsequent simulation was conducted in the post-percolation stage. The correlation between the permeability and the packing density does not demonstrate a clear pattern in the L20 group. Fig. 10 (b) presents the permeation simulation results with an individual rod length of 6lu. The percolation threshold of the network was $P_g = 1.07\%vol$ from the EM- P_g function, and the subcritical threshold was $P_s = 0.79\%vol$ from the EM- P_s function. Comparing with the L20 group, the statistics flocculation of the L6 simulation is considerably outstanding especially when the volume fraction is lower than the percolation threshold. A general trend that increased network volume fraction raises the permeability can be noticed, and the permeability under the same network content is analogous with the L20 group. However, one outstanding difference is that the permeability development of the L6 group was strongly influenced by the packing density except in the non-representative RLP2 porous medium. A pattern can be observed that the increased packing density

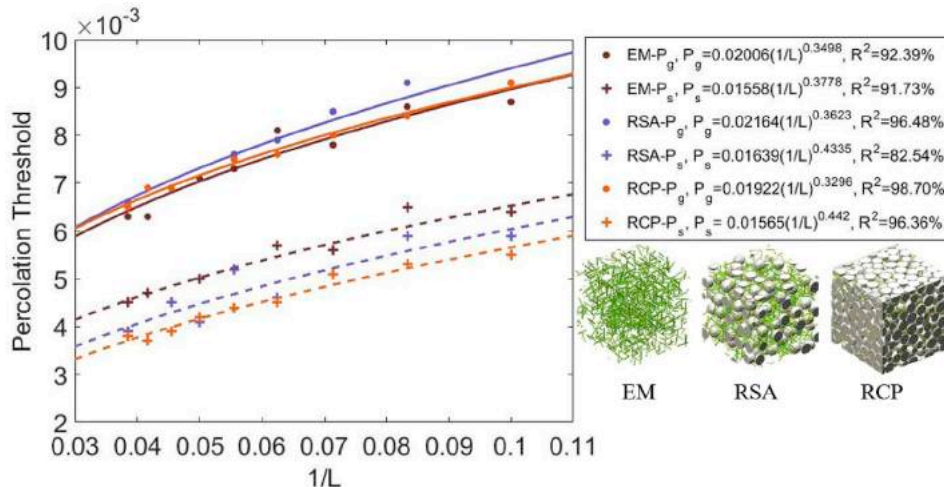


Fig. 9. Percolation threshold and sub-critical percolation threshold development regarding varied individual rod length.

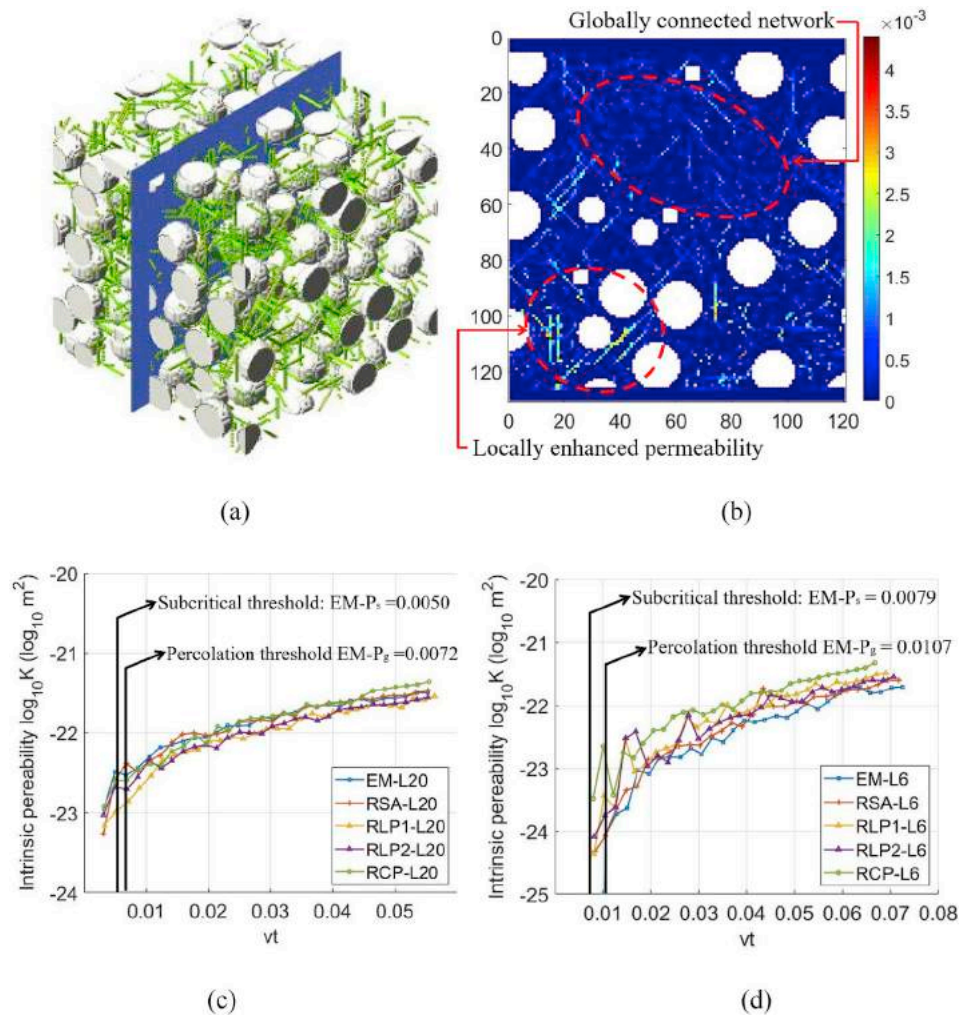


Fig. 10. (a) Cross-section of a network placed in the RSA porous medium. (b) Cross-sectional speed distribution in the network under permeation. (c) Result of L20 permeation simulations. (d) Result of L6 permeation simulations.

caused the raised permeability. This pattern corresponds well with P_s development in the percolation analysis. Experimentally realizing the permeation test through connected CNT is extremely difficult, if not impossible. However, the previous experiment of permeation through porous media with ultra-low porosity can provide a vision of a similar picture. According to the available reference [81], water permeability with a degree of magnitude of $10^{-20} m^2$ was observed in a medium with a confirmative porosity of 0.1170, and the water permeability was too small to measure with the porosity of 0.0726. In comparison, this work presents an estimated permeability of 10^{-23} – $10^{-21} m^2$ with a network content of 0.01–0.08.

The particle size of the porous medium was 8 μ , and the major pore size of the packed pore structure was in the same degree of magnitude. The rod length in L20 group exceeds most of the pore size, therefore the permeability was more influenced by the cluster of the pores rather than the individual pore. Therefore, the resulted permeability contribution from the individual rod was more significant. On the other hand, the L6 group was in the same degree of magnitude of the pore size. The possibility of the rod cluster formation in individual pore was therefore increased. In this sense, the influence of the porous medium was enhanced by the local formation of the network. This microscale influences eventually led to the macroscale observation of the illustrated pattern of permeability development. The above study indicates that there may exist a length threshold to distinguish the dependence of the pore structure on the permeability of the rod network within.

3.4. Formation factor analysis and discussion with experimental results

Table 3 presents the void ratio (P_V) of the five porous media and the base flux (J_0) through these media from the diffusion simulation. It can be noticed that the base flux strictly follows a size order according to the void ratio, and a high void ratio leads to an increased amount of the base flux. Fig. 11 presents the formation factor development as a means to evaluate electrical conductivity development. The influence of the void ratio on the formation factor development of the EM-L6, RSA-L6, EM-L20 and RSA-L20 simulation indicates that higher void ratio leads to a faster recovery of the conductivity. The sensitivity to the void ratio in the three packed porous media is less than that in the two unpacked medium. More importantly, Archie's law [48,52] as given by Eq. (15) is recovered with considerably high coefficients of determination.

$$F = av_t^{-m} \quad (15)$$

Where a is the tortuosity factor, m is the cementation exponent and the vt is the network content. The tortuosity factor obtained from the EM-

Table 3

Base properties of the formation factor analysis.

	EM	RSA	RLP2	RLP1	RCP
Void Ratio (P_V)	100%	82.43%	63.94%	49.38%	38.08%
Base flux (J_0)	8.36e-18	2.93e-18	1.23e-18	1.13e-18	1.04e-18

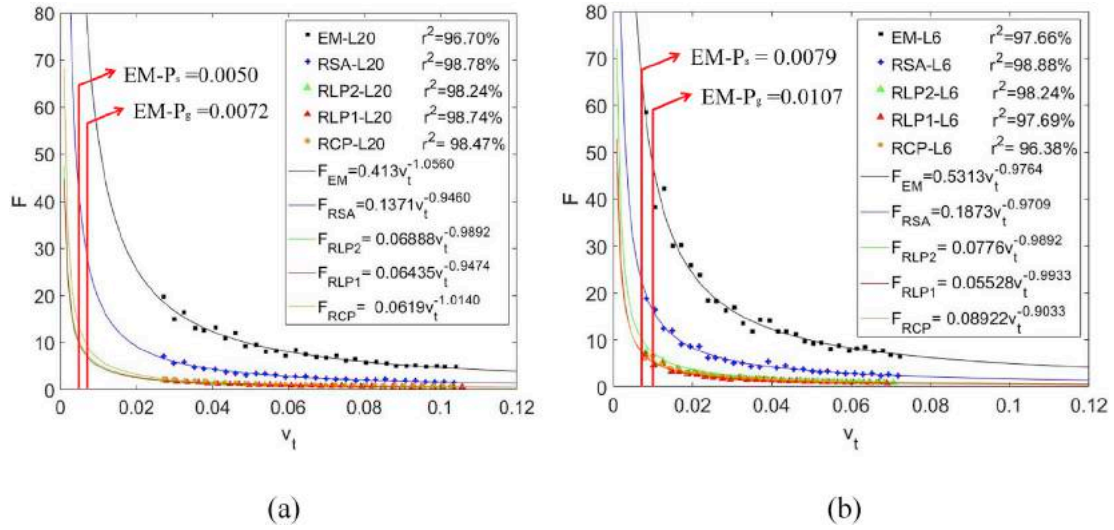


Fig. 11. Formation factor analysis of (a) L20 samples and (b) L6 samples.

L20, RSA-L20, RLP1-L20 and RCP-L20 networks were 0.413, 0.1371, 0.06435 and 0.0619, respectively. The cementation exponent obtained from the EM-L20, RSA-L20, RLP1-L20 and RCP-L20 networks were 1.0560, 0.9460, 0.9882 and 1.0140, respectively.

When comparing the RCP-RSA-EM simulations, both the L20 group and the L6 group demonstrates that the increased packing density led to a reduction of the tortuosity factor and decreased formation factor under the same network content. This result indicates that the packed porous medium can enhance the conductivity of the network. Similar to the result of permeation simulation, extended rod length altered the magnitude order of the formation factor in the three packed medium. In the L6 simulations, the formation factor with the same network content presents a magnitude order following RCP-RLP1-RLP2-RSA-EM from low to high, which is exactly the magnitude order of the packing density of the media. On the other hand, the magnitude order becomes RLP1-RLP2-RCP-RSA-EM in the L20 simulations. This result indicates that the length influence reflected by the permeation simulation still exist in the diffusion simulation, and the affected porous medium are exactly the three packed media. Therefore, the above result leads to a conclusion that shortened length of the rod or CNT introduces the local influence of the individual pore in a packed porous medium during the formation of the electrical conductivity.

The electrical resistivity (ρ_e) development of the system reflected by the formation factor was given by Eq. (16), [48,51]. It was assumed that the electron migration path was the same as the diffusive path.

$$F = \frac{D_0}{D_e} = \frac{\rho_e}{\rho_0} \quad (16)$$

Where F is the formation factor, D_0 is the diffusion coefficient of the bulk, D_e is the diffusion coefficient of the network in pores, ρ_e is the resistivity of the network and ρ_0 is the resistivity of the bulk conductive phase. Experimentally, the transport property of the CNT network in cement was reflected by the electrical resistivity to the CNT volumetric fraction as presented by Fig. 12. One major problem of the experimental evaluation of the conductive network within a porous medium is that the conductivity can be contributed by phases other than the CNT network. In the case of the example experiment, the conductivity was contributed by both the pore solution and the CNT network.

The cementation component in the experimental curve is $m = 1.062$ with a coefficient of determination of 91.47%. In comparison, the cementation component was reported to be 1.69–2.86 [48]. The decrement of the cementation component in this study indicates that the conductive network in the rod-particle composite was more integrated.

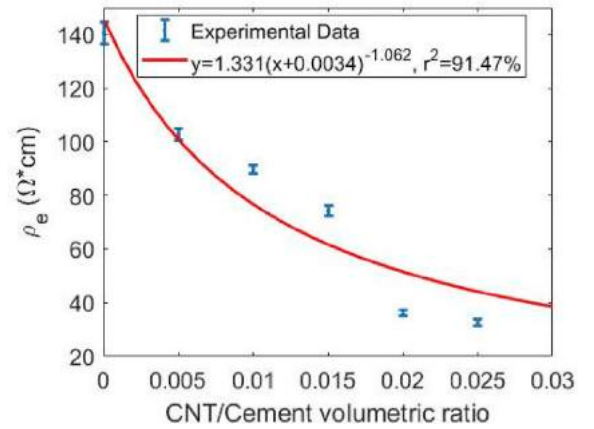


Fig. 12. Experimentally measured electric resistivity development in fresh mortar.

Through the comparison between the formation factor analysis and the example experiment, it can be noticed that the increased CNT volumetric fraction led to a decreased electric resistivity obeying Archie's law. However, one major difference between the simulation and the experiment is that the simulated curve does not have an intersection with y-axis. As previously discussed, the system of the cementitious composite had conductive phase other than the CNT network and there still existed conductivity even when the CNT content was zero, which is numerically reflected by the intersection with y-axis. Treating the offset of the x value in the function as the equivalent CNT volumetric fraction, the regressed function from the experiments indicates that the contribution of the pore solution is equivalent to CNT occupying 0.0034 (0.34%) of the volume. In a porous medium, the previous study concluded [21–23] that pores occupying 10–20%vol is sufficient for each individual pore to form a global interconnection, and the lowest void ratio through random packing was well acknowledged to be 36% [67]. As a result, the global connection of the pore solution can naturally be formed even through 0.34%vol is lower than the percolation threshold of the CNT network. In this sense, the electric resistivity measured in the fresh cementitious composite cannot directly reflect the CNT network formation within, and the simulation-based study is of great necessity to evaluate the formation of the conductivity of the CNT in a composite system.

Eq. (17) presents a mean to quantitatively evaluate the electrical

conductivity of the network with available formation factor and bulk conductivity. In the system of the example experiment, the determination of the tortuosity factor(a) can further help to identify the microscale contact resistivity caused by the covering of the hydration product on the surface of the CNT as illustrated by Fig. 13. Here, we applied the tortuosity factor obtained from the RCP-L20 simulation and rearrange Eq. (16) to Eq. (17). The experimentally obtained electrical resistivity is given by Eq. (18) after equalisation

$$\rho_{e, \text{simulation}} = \rho_0 F_{\text{RCP-L20}} = \rho_0 \cdot 0.0619 v_t^{-1.0140} \quad (17)$$

$$\rho_{e, \text{experiment}} = 1.331 v_t^{-1.062} \quad (18)$$

Through the comparison between Eqs. (17) and (18), It can be estimated that an elementary resistivity of 21.5Ω·cm is necessary to make the RCP-L20 simulation representative for the experiment, and this value is about 28 times of the electrical resistivity of the bulk CNT (0.78 Ω cm). However, the improvement of the combination between simulation and experiment to investigate the true feature of the conductive network in porous media still requires the development of more detailed 3D modelling techniques and advanced testing methods under strictly controlled variables.

4. Summary

In this paper, we demonstrated an originally proposed percolation-permeation-diffusion simulation and analysis scheme. An investigation was conducted on the connectivity and conductivity development of the rod networks in differently packed media. The main findings of the study are concluded as follows:

- A volume size of $120 \times 120 \times 120 \mu\text{m}^3$ was sufficient to fulfil the representativity requirement of the EM, RSA, RLP1 and the RCP composite with rod length up to 22 μm . The composite formed under the unstable RLP2 packing states required a sample size larger than $120 \times 120 \times 120 \mu\text{m}^3$ for representativity. The heterogeneity of the non-representative samples caused increased connectivity and the conductivity when the length of the rod was shortened. The 10^{-4} chi-square criterion is stricter than the criteria in the previous image-based study. The non-representative sample can lead to statistical fluctuation as demonstrated by the RLP2 simulations
- EM-L6 network resulted in a percolation threshold of 0.0107 and a subcritical threshold of 0.0079. EM-L20 network resulted in a percolation threshold of 0.0072 and a subcritical threshold of 0.0050. On the other hand, RCP-L6 network resulted in a percolation threshold of 0.0106 and a subcritical threshold of 0.0071. RCP-L20 network resulted in a percolation threshold of 0.0072 and a subcritical threshold of 0.0042. The increased packing fraction was

in favour of the fraction of connection development of the rod network, but the percolation threshold was only minorly influenced. Increased rod length led to reduction of the percolation threshold and the subcritical threshold. More importantly, the subcritical percolation was strongly influenced by the particle packing states, and reduced packing density resulted in a raised subcritical threshold. The connected path of the network through the macroscopic composite was harder to form in a loosely packed porous medium.

- In the permeation simulation with L6 networks, intrinsic permeability with a range of 10^{-24} – 10^{-21} m^2 was obtained with rod content of 0.01–0.08. RCP-L6 network demonstrated the highest permeability result, which is about 5 times higher than the result of EM-L6 network under the same rod content. Permeability of the network in composite increased with the network content. The non-representative RLP2-L6 networks demonstrated an obvious fluctuation in terms of data development. L20 networks resulted in intrinsic permeability with a range of 10^{-23} – 10^{-21} m^2 from the simulation with a rod content of 0.01–0.08. No clear pattern of the permeability variation between RCP-L20 networks and EM-L20 networks was observed. Decreased rod length led to an increased sensitivity of the network to the porous medium and the reportativity. In the composite with extended rod length, the influence from the particle packing density was minor. A strong influence from the packing density on the permeability was observed when the rod length was shortened, and the increased packing density resulted in enhanced permeability. There may exist a rod length threshold in the degree of magnitude of the pore size to trigger the influence of the packing states.
- Numerically, Archie's law was recovered from the formation factor simulation, and it was found that the form of the function can as well describe the resistivity development of the experimental system. The tortuosity factor obtained from the EM-L20, RSA-L20, RLP1-L20 and RCP-L20 networks were 0.413, 0.1371, 0.06435 and 0.0619, respectively. The cementation exponent obtained from the EM-L20, RSA-L20, RLP1-L20 and RCP-L20 networks were 1.0560, 0.9460, 0.9882 and 1.0140, respectively. An increased network content led to a reduction of the formation factor. Higher packing density caused decreased formation factor in all the representative samples. Shortened rod length introduced the local influence of the individual pore in a packed porous medium on the formation of the electrical conductivity. The experiment demonstrated a similar trend that increased CNT content reduced the electrical resistivity of the CNT-cement composite. The experimental cementation component was $m = 1.062$. The covering of the hydration product on the CNT surface could magnify the elementary resistivity of the CNT network to a magnification of tens times.

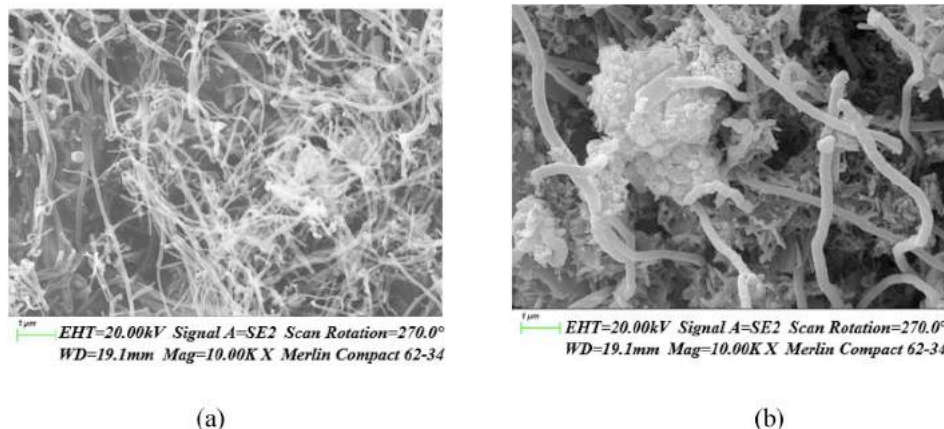


Fig. 13. (a) Bulk CNTs dispersed in the liquid. (b) CNT covered with hydration product in the composite.

Declaration of competing interest

The authors declare that they have no conflict of interest.

CRediT authorship contribution statement

Mingzhi Wang: Conceptualization, Methodology, Software, Validation, Visualization, Writing - original draft, Writing - review & editing. **Yushi Liu:** Investigation, Resources. **Beimeng Qi:** Investigation. **Abir Al-Tabbaa:** Supervision. **Wei Wang:** Project administration.

Appendix A. Supplementary data

Supplementary data to this article can be found online at <https://doi.org/10.1016/j.compositesb.2020.107837>.

References

- Ajayan PM, Lijima S. Smallest carbon nanotube. *Nature* 1992;358:23. <https://doi.org/10.1038/358023a0>.
- PourAkbar Saffar K, Sudak LJ, Federico S. A biomechanical evaluation of CNT-grown bone. *J Biomed Mater Res* 2016;104:465–75. <https://doi.org/10.1002/jbm.a.35582>.
- Rana MM, Ibrahim DS, Asyraf MRM, Jarin S, Tomal A. A review on recent advances of CNTs as gas sensors. *Sens Rev* 2017;37:127–36. <https://doi.org/10.1108/SR-10-2016-0230>.
- Fiedler B, Gojny FH, Wichmann MHG, Bauhofer W, Schulte K. Can carbon nanotubes be used to sense damage in composites? *Ann Chim Sci Des Mater* 2004;29:81–94. <https://doi.org/10.3166/acsm.29.6.81-94>.
- Dalkilic AS, Küçükıldırım BO, Akdoğan Eker A, Çebi A, Tapan S, Jumholkul C, et al. Experimental investigation on the viscosity of Water-CNT and Antifreeze-CNT nanofluids. *Int Commun Heat Mass Tran* 2017;80:47–59. <https://doi.org/10.1016/j.icheatmasstransfer.2016.11.011>.
- Chen X, Oh W, Lim T. Graphene- and CNTs-based carbocatalysts in persulfates activation: material design and catalytic mechanisms. *Chem Eng J* 2018;354:941–76. <https://doi.org/10.1016/j.cej.2018.08.049>.
- Lee HS, Balasubramanian B, Gopalakrishna GVT, Kwon SJ, Karthick SP, Saraswathy V. Durability performance of CNT and nanosilica admixed cement mortar. *Construct Build Mater* 2018;159:463–72. <https://doi.org/10.1016/j.conbuildmat.2017.11.003>.
- Peng B, Takai K, Razavi-Khosroshahi H, Salmawy MSE, Fuji M. Effect of CNTs on morphology and electromagnetic properties of non-firing CNTs/silica composite ceramics. *Adv Powder Technol* 2018;29:1865–70. <https://doi.org/10.1016/j.appt.2018.04.024>.
- Liu Y, Wang M, Tian W, Qi B, Lei Z, Wang W. Ohmic heating curing of carbon fiber/carbon nanofiber synergistically strengthening cement-based composites as repair/reinforcement materials used in ultra-low temperature environment. *Compos Part A Appl Sci Manuf* 2019;125. <https://doi.org/10.1016/j.compositesa.2019.105570>.
- Sandler JKW, Kirk JE, Kinloch IA, Shaffer MSP, Windle AH. Ultra-low electrical percolation threshold in carbon-nanotube-epoxy composites. *Polymer (Guildf)* 2003;44:5893–9. [https://doi.org/10.1016/S0032-3861\(03\)00539-1](https://doi.org/10.1016/S0032-3861(03)00539-1).
- Wichmann MHG, Sumfleth J, Fiedler B, Gojny FH, Schulte K. Multiwall carbon nanotube/epoxy composites produced by a masterbatch process. *Mech Compos Mater* 2006;42:395–406. <https://doi.org/10.1007/s11029-006-0050-3>.
- Gojny FH, Wichmann MHG, Fiedler B, Kinloch IA, Bauhofer W, Windle AH, et al. Evaluation and identification of electrical and thermal conduction mechanisms in carbon nanotube/epoxy composites. *Polymer (Guildf)* 2006;47:2036–45. <https://doi.org/10.1016/j.polymer.2006.01.029>.
- Vargas-Lara F, Douglas JF. Confronting the complexity of CNT materials. *Soft Matter* 2015;11:4888–98. <https://doi.org/10.1039/c5sm00912j>.
- Li J, Ma PC, Chow WS, To CK, Tang BZ, Kim JK. Correlations between percolation threshold, dispersion state, and aspect ratio of carbon nanotubes. *Adv Funct Mater* 2007;17:3207–15. <https://doi.org/10.1002/adfm.200700065>.
- Ang EYM, Ng TY, Yeo J, Lin R, Liu Z, Geethalakshmi KR. Effects of CNT size on the desalination performance of an outer-wall CNT slit membrane. *Phys Chem Chem Phys* 2018;20:13896–902. <https://doi.org/10.1039/c8cp01191e>.
- Kayama Y. Cellular automata in fractal arrangement. *Artif Life Robot* 2018;23:1–7. <https://doi.org/10.1007/s10015-018-0448-8>.
- Raabe D. Overview of the lattice Boltzmann method for nano- and microscale fluid dynamics in materials science and engineering. *Model Simulat Mater Sci Eng* 2004;12:R13–46. <https://doi.org/10.1088/0965-0393/12/6/R01>.
- Bonnet P, Sireude D, Garnier B, Chauvet O. Thermal properties and percolation in carbon nanotube-polymer composites. *Appl Phys Lett* 2007;91. <https://doi.org/10.1063/1.2813625>. 2005–8.
- Haghgo M, Ansari R. Prediction of electrical conductivity of carbon fiber-carbon nanotube-reinforced polymer hybrid composites. *Compos Part B* 2019;167:728–35. <https://doi.org/10.1016/j.compositesb.2019.03.046>.
- Kirkpatrick S. *Percolation and Conduction* 1973;45.
- Ye G. Percolation of capillary pores in hardening cement pastes. *Cement Concr Res* 2005;35:167–76. <https://doi.org/10.1016/j.cemconres.2004.07.033>.
- Garboczi EJ. Percolation phase diagrams for multi-phase models built on the overlapping sphere model. *Phys Stat Mech Appl* 2016;442:156–68. <https://doi.org/10.1016/j.physa.2015.09.014>.
- Bentz DP. Capillary porosity depercolation/repercolation in hydrating cement pastes via low-temperature calorimetry measurements and CEMHYD3D modeling. *J Am Ceram Soc* 2006;89:2606–11. <https://doi.org/10.1111/j.1551-2916.2006.01102.x>.
- Mao X, Liu Y, Guan W, Yueli F. Experimental and numerical simulation on the influence of anisotropic fracture network deformation to shale gas percolation. 2018.
- Zahasky C, Thomas D, Matter J, Maher K, Benson SM. Multimodal imaging and stochastic percolation simulation for improved quantification of effective porosity and surface area in vesicular basalt. *Adv Water Resour* 2018;121:235–44. <https://doi.org/10.1016/j.advwatres.2018.08.009>.
- Newman MEJ, Ziff RM. Efficient Monte Carlo algorithm and high-precision results for percolation. *Phys Rev Lett* 2000;85:4104–7. <https://doi.org/10.1103/PhysRevLett.85.4104>.
- Mietta JL, Negri RM, Tamborenea PI. Numerical simulations of stick percolation: application to the study of structured magnetorheological elastomers. *J Phys Chem C* 2014;118:20594–604. <https://doi.org/10.1021/jp504197w>.
- von Neumann J. The general and logical theory of automata. In: Jeffress LA, editor. *Syst. Behav. Sci. A sourceb*. New York: John Wiley & Sons; 2017. p. 97–107.
- Khanjary M, Sabaei M, Meybodi MR. A percolation algorithm based on cellular automata. *IEEE Int Conf Electro Inf Technol* 2015. <https://doi.org/10.1109/EIT.2015.7293431>. 2015-June:472–7.
- Najafi MN. Percolation transition in two dimensional electron gas: a cellular automaton model. *Solid State Commun* 2018;284–286:84–7. <https://doi.org/10.1016/j.ssc.2018.08.006>.
- Andrianov IV, Danishevs'ky VV, Kalamkarov AL. Analysis of the effective conductivity of composite materials in the entire range of volume fractions of inclusions up to the percolation threshold. *Compos B Eng* 2010;41:503–7. <https://doi.org/10.1016/j.compositesb.2010.05.001>.
- Prandtl L, Tietjens OG. *Applied hydro- and aeromechanics*. London: McGraw-Hill; 1934.
- Landau LD, Lifshitz EM. *Fluid mechanics*. Oxford: Pergamon; 1959.
- Powell MS, Weerasekera NS, Cole S, Laroche RD, Favier J. DEM modelling of liner evolution and its influence on grinding rate in ball mills. *Miner Eng* 2011;24:341–51. <https://doi.org/10.1016/j.mineng.2010.12.012>.
- Thakur SC, Ooi JY, Ahmadian H. Scaling of discrete element model parameters for cohesionless and cohesive solid. *Powder Technol* 2016;293:130–7. <https://doi.org/10.1016/j.powtec.2015.05.051>.
- Swift MR, Osborn WR, Yeomans JM. Lattice Boltzmann simulation of non-ideal fluids. *Phys Rev Lett* 1995;75:830.
- Matuttis Hans-Georg, Chen Jian. *Understanding the discrete element method*. first ed. Singapore: John Wiley & Sons; 2014.
- Ali MA, Umer R, Khan KA, Cantwell WJ. XCT-scan assisted flow path analysis and permeability prediction of a 3D woven fabric. *Compos B Eng* 2019;176. <https://doi.org/10.1016/j.compositesb.2019.107320>. 107320.
- Nazari A, Riahi S. Prediction split tensile strength and water permeability of high strength concrete containing TiO₂ nanoparticles by artificial neural network and genetic programming. *Compos B Eng* 2011;42:473–88. <https://doi.org/10.1016/j.compositesb.2010.12.004>.
- Turner DZ, Hjelmstad KD. Determining the 3D permeability of fibrous media using the Newton method. *Compos B Eng* 2005;36:609–18. <https://doi.org/10.1016/j.compositesb.2005.01.009>.
- Zhang M, Ye G, Van Breugel K. Modeling of ionic diffusivity in non-saturated cement-based materials using lattice Boltzmann method. *Cement Concr Res* 2012;42:1524–33. <https://doi.org/10.1016/j.cemconres.2012.08.005>.
- Mino Y, Hasegawa A, Shinto H, Matsuyama H. Lattice-Boltzmann flow simulation of an oil-in-water emulsion through a coalescing filter: effects of filter structure. *Chem Eng Sci* 2018;177:210–7. <https://doi.org/10.1016/j.ces.2017.11.027>.
- Zhang LZ. A lattice Boltzmann simulation of mass transport through composite membranes. *AIChE J* 2014;60:3925–38. <https://doi.org/10.1002/aic.14564>.
- Mu Y-T, Weber AZ, Gu Z-L, Tao W-Q. Mesoscopic modeling of transport resistances in a polymer-electrolyte fuel-cell catalyst layer: analysis of hydrogen limiting currents. *Appl Energy* 2019;255. <https://doi.org/10.1016/j.apenergy.2019.113895>. 113895.
- Zhang M, Ye G, Van Breugel K. Microstructure-based modeling of permeability of cementitious materials using multiple-relaxation-time lattice Boltzmann method. *Comput Mater Sci* 2013;68:142–51. <https://doi.org/10.1016/j.commatsci.2012.09.033>.
- Kang Q, Zhang D, Chen S. Simulation of dissolution and precipitation in porous media. *J Geophys Res Solid Earth* 2003;108:2505. <https://doi.org/10.1029/2003jb002504>.
- Kang Q, Lichtner PC, Viswanathan HS, Abdel-Fattah AI. Pore scale modeling of reactive transport involved in geologic CO₂ sequestration. *Transport Porous Media* 2010;82:197–213. <https://doi.org/10.1007/s11242-009-9443-9>.
- Sallehi H, Ghods P, Isgor OB. Formation factor of fresh cementitious pastes. *Cement Concr Compos* 2018;91:174–88. <https://doi.org/10.1016/j.cemconcomp.2018.05.011>.
- Qin Z, Pan H, Ma H, Konaté AA, Hou M, Luo S. Fast prediction method of Archie's cementation exponent. *J Nat Gas Sci Eng* 2016;34:291–7. <https://doi.org/10.1016/j.jngse.2016.06.070>.
- Promentilla MAB, Sugiyama T, Hitomi T, Takeda N. Quantification of tortuosity in hardened cement pastes using synchrotron-based X-ray computed

- microtomography. *Cement Concr Res* 2009;39:548–57. <https://doi.org/10.1016/j.cemconres.2009.03.005>.
- [51] Latour LL, Kleinberg RL, Mitra PP, Sotak CH. Pore-size distributions and tortuosity in heterogeneous porous media. *J Magn Reson, Ser A* 1995;112:83–91. <https://doi.org/10.1006/jmra.1995.1012>.
- [52] Archie GE. The electrical resistivity log as an aid in determining some reservoir characteristics. *Petrol Tech* 1942;54–62. <https://doi.org/10.2118/942054-G>.
- [53] Willis JR. Variational and related methods for the overall properties of composites. *Adv Appl Mech* 1981;21:1–78. [https://doi.org/10.1016/S0065-2156\(08\)70330-2](https://doi.org/10.1016/S0065-2156(08)70330-2).
- [54] Gitman IM, Gitman MB, Askes H. Quantification of stochastically stable representative volumes for random heterogeneous materials. *Arch Appl Mech* 2006;75:79–92. <https://doi.org/10.1007/s00419-005-0411-8>.
- [55] Ukrainczyk N, Koenders E a B. Representative elementary volumes for 3D modeling of mass transport in cementitious materials. *Model Simulat Mater Sci Eng* 2014;22:35001. <https://doi.org/10.1088/0965-0393/22/3/035001>.
- [56] Lurie SA, Volkov-Bogorodskiy DB, Menshykov O, Solyaev Y, Aifantis E. Modeling the effective mechanical properties of “fuzzy fiber” composites across scales length. *Compos B Eng* 2018;142:24–35. <https://doi.org/10.1016/j.compositesb.2017.12.029>.
- [57] Mazzucco G, Kotta G, Pomaro B, Salomoni VA, Faleschini F. Elastoplastic-damaged meso-scale modelling of concrete with recycled aggregates. *Compos B Eng* 2018;140:145–56. <https://doi.org/10.1016/j.compositesb.2017.12.018>.
- [58] Kim DW, Lim JH, Yu J. Efficient prediction of the electrical conductivity and percolation threshold of nanocomposite containing spherical particles with three-dimensional random representative volume elements by random filler removal. *Compos B Eng* 2019;168:387–97. <https://doi.org/10.1016/j.compositesb.2019.03.038>.
- [59] Bargmann S, Klusemann B, Markmann J, Schnabel JE, Schneider K, Soyarslan C, et al. Generation of 3D representative volume elements for heterogeneous materials: a review. *Prog Mater Sci* 2018;96:322–84. <https://doi.org/10.1016/j.pmatsci.2018.02.003>.
- [60] Harper LT, Qian C, Turner TA, Li S, Warrior NA. Representative volume elements for discontinuous carbon fibre composites - Part 1: boundary conditions. *Compos Sci Technol* 2012;72:225–34. <https://doi.org/10.1016/j.compscitech.2011.11.006>.
- [61] Harper LT, Qian C, Turner TA, Li S, Warrior NA. Representative volume elements for discontinuous carbon fibre composites - Part 2: determining the critical size. *Compos Sci Technol* 2012;72:204–10. <https://doi.org/10.1016/j.compscitech.2011.11.003>.
- [62] Wang M, Al-Tabbaa A, Wang W. Improving discrete particle packing models for the microstructural formation simulation of Portland cement. *Construct Build Mater* 2019;229. <https://doi.org/10.1016/j.conbuildmat.2019.116841>.
- [63] de Korte aCJ, Brouwers HJH. Random packing of digitized particles. *Powder Technol* 2013;233:319–24. <https://doi.org/10.1016/j.powtec.2012.09.015>.
- [64] Dong K, Yang R, Zou R, Yu a. Role of interparticle forces in the formation of random loose packing. *Phys Rev Lett* 2006;96. <https://doi.org/10.1103/PhysRevLett.96.145505>.
- [65] Xu WX, Chen HS. Microstructural characterization of fresh cement paste via random packing of ellipsoidal cement particles. *Mater Char* 2012;66:16–23. <https://doi.org/10.1016/j.matchar.2012.01.012>.
- [66] Yang X, Wang F, Yang X, Zhu F, Chi B. Quantity and shape modification for random-fractal-based 3D concrete meso-simulation. *Powder Technol* 2017;320:161–78. <https://doi.org/10.1016/j.powtec.2017.07.031>.
- [67] Wang M, Al-Tabbaa A, Wang W. Improving discrete particle packing models for the microstructural formation simulation of Portland cement. *Construct Build Mater* 2019;229. <https://doi.org/10.1016/j.conbuildmat.2019.116841>.
- [68] MacDonald JR. Some simple isothermal equations of state. *Rev Mod Phys* 1966;38:669–79. <https://doi.org/10.1103/RevModPhys.38.669>.
- [69] Chen H. *Lattice Boltzmann*; 1996.
- [70] Qian YH, D'Humières D, Lallemand P. Lattice BGK models for Navier-Stokes equation. *Europhys Lett* 1992;17:479–84. <https://doi.org/10.1209/0295-5075/17/6/001>.
- [71] Zhou C, Ren F, Wang Z, Chen W, Wang W. Why permeability to water is anomalously lower than that to many other fluids for cement-based material? *Cement Concr Res* 2017;100:373–84. <https://doi.org/10.1016/j.cemconres.2017.08.002>.
- [72] Kang Q, Lichtner PC, Zhang D. Lattice Boltzmann pore-scale model for multicomponent reactive transport in porous media. *J Geophys Res* 2006;111. <https://doi.org/10.1029/2005JB003951>.
- [73] Fick A. On liquid diffusion. *J Membr Sci* 1995;100:33–8. [https://doi.org/10.1016/0376-7388\(94\)00230-V](https://doi.org/10.1016/0376-7388(94)00230-V).
- [74] Wang Mingzhi. Numerical modelling of the kinetics and microstructural development of carbonated magnesia-based cements (Doctoral dissertation). University of Cambridge; 2017.
- [75] Xie N, Shi X, Feng D, Kuang B, Li H. Percolation backbone structure analysis in electrically conductive carbon fiber reinforced cement composites. *Compos B Eng* 2012;43:3270–5. <https://doi.org/10.1016/j.compositesb.2012.02.032>.
- [76] Dettlaff-Weglikowska U, Kaempgen M, Hornbostel B, Skakalova V, Wang J, Liang J, et al. Conducting and transparent SWNT/polymer composites. *Phys Status Solidi Basic Res* 2006;243:3440–4. <https://doi.org/10.1002/pssb.200669188>.
- [77] Liu L, Matitsine S, Gan YB, Chen LF, Kong LB, Rozanov KN. Frequency dependence of effective permittivity of carbon nanotube composites. *J Appl Phys* 2007;101. <https://doi.org/10.1063/1.2728765>.
- [78] Bai JB, Allaoui A. Effect of the length and the aggregate size of MWNTs on the improvement efficiency of the mechanical and electrical properties of nanocomposites - experimental investigation. *Compos Part A Appl Sci Manuf* 2003;34:689–94. [https://doi.org/10.1016/S1359-835X\(03\)00140-4](https://doi.org/10.1016/S1359-835X(03)00140-4).
- [79] Yu A, Itkis ME, Bekyarova E, Haddon RC. Effect of single-walled carbon nanotube purity on the thermal conductivity of carbon nanotube-based composites. *Appl Phys Lett* 2006;89. <https://doi.org/10.1063/1.2357580>.
- [80] Haghighi M, Ansari R, Nankali M. Analytical formulation for electrical conductivity and percolation threshold of epoxy multiscale nanocomposites reinforced with chopped carbon fibers and wavy carbon nanotubes considering tunneling resistivity. *Compos Part A* 2019;126. <https://doi.org/10.1016/j.compositesa.2019.105616>.
- [81] Zhou C, Chen W, Wang W, Skoczylas F. Indirect assessment of hydraulic diffusivity and permeability for unsaturated cement-based material from sorptivity. *Cement Concr Res* 2016;82:117–29. <https://doi.org/10.1016/j.cemconres.2016.01.002>.